



# Overcoming diffusion limitations in supercapacitors using layered electrodes

R. Drummond<sup>a,\*</sup>, C. Huang<sup>b</sup>, P.S. Grant<sup>b</sup>, S.R. Duncan<sup>a</sup>

<sup>a</sup> Department of Engineering Science, University of Oxford, 17 Parks Road, OX1 3PJ, Oxford, United Kingdom

<sup>b</sup> Department of Material Science, University of Oxford, Parks Road, OX1 3PH, Oxford, United Kingdom

## HIGHLIGHTS

- An electrochemical supercapacitor model for layered electrodes is pro-posed.
- The model is validated against experimental impedance data.
- Electrode layering is shown to increase ion mobility across the elec-trode.
- Layered electrodes extend the frequency range for charge storage in supercapacitors.

## ARTICLE INFO

### Index Terms:

Supercapacitors  
Electric double layer structured electrodes  
Electrochemical modelling

## ABSTRACT

The impact of multi-layered electrode microstructures on the dynamic capacitance of electrochemical double layer supercapacitors is investigated. An electrochemical model that describes ion diffusion and double layer dynamics across the layered electrodes is first developed and then matched to experimental data. With TiO<sub>2</sub> particulate and carbon nanotube layered electrodes, two knee frequencies were observed in the real and imaginary capacitance plots in both experiment and model simulations. These two knee frequencies resulted in an increase in real capacitance at high frequencies ( $\omega \approx 10^0 - 10^2 \text{ rad s}^{-1}$ ) but a reduction at lower frequencies ( $\omega \approx 10^{-2} \text{ rad s}^{-1}$ ), with the response being largely insensitive to the relative layer thicknesses. The increased capacity at high frequencies was due to increased ion mobility across the electrodes caused by the layering, allowing diffusion limitations of identical homogeneous electrodes to be overcome. These results imply the suitability of layered electrodes for applications with highly dynamic charge profiles and/or relatively thick electrodes.

## 1. Introduction

Supercapacitors with approximately ten times higher power densities (5–50 kW kg<sup>-1</sup>) and significantly longer cycle lives (>10<sup>4</sup> cycles) but lower energy densities (3–40 Wh kg<sup>-1</sup>) than Li ion batteries are attractive for alternating current (AC) ripple filtering, hybrid electric vehicles and meeting peak power demands in electrical grid storage [21, 24,27]. Consisting of a porous separator sandwiched between two identical electrodes and immersed in a liquid electrolyte, supercapacitors predominantly store charge by fast electrostatic adsorption of electrolyte ions onto the surface of the oppositely charged electrodes, as illustrated in Fig. 1. The main benefit of storing charge on the electrode surface in this way is that it leads to high power densities, being

principally limited only by the mobility of the ions across the separator and through the porous electrode. However, surface only energy storage leads to relatively low energy densities, which has motivated the development of active materials with exceptionally high surface areas (500–2000 m<sup>2</sup> g<sup>-1</sup>) for supercapacitor electrodes, including activated carbon [5], carbon nanotubes (CNTs) [33], graphene [27] and metal oxide nanomaterials [19].

In contrast to conventional supercapacitor electrodes that are random mixtures of active, electron conducting and binder materials, this paper considers the modelling and design of supercapacitors with structured electrodes. The term structured electrodes here refers to spatially heterogeneous electrodes composed of layers with different materials [20], as illustrated in Fig. 2. Recent experimental data has

\* Corresponding author.

E-mail addresses: [ross.drummond@eng.ox.ac.uk](mailto:ross.drummond@eng.ox.ac.uk) (R. Drummond), [ann.huang@materials.ox.ac.uk](mailto:ann.huang@materials.ox.ac.uk) (C. Huang), [patrick.grant@materials.ox.ac.uk](mailto:patrick.grant@materials.ox.ac.uk) (P.S. Grant), [stephen.duncan@eng.ox.ac.uk](mailto:stephen.duncan@eng.ox.ac.uk) (S.R. Duncan).

<https://doi.org/10.1016/j.jpowsour.2019.04.107>

Received 25 January 2019; Received in revised form 5 April 2019; Accepted 28 April 2019

Available online 4 June 2019

0378-7753/© 2019 The Authors. Published by Elsevier B.V. This is an open access article under the CC BY license (<http://creativecommons.org/licenses/by/4.0/>).

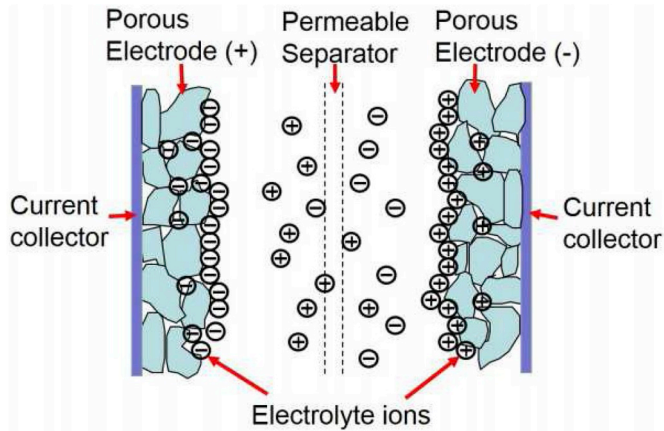


Fig. 1. A schematic diagram of a supercapacitor at the charged state.

shown that layering can give attractive combinations of energy and power density for solid-state supercapacitors [20] and Li-ion batteries [8], although unambiguously resolving the underlying reasons for improved behaviour is complex. Here, a model is developed to better understand and probe the underlying ionic mobility in structured electrodes and its links to energy storage performance, revealing the benefits of structured electrodes for applications where ionic diffusion limitations dominate, such as in high frequency charging and the filtering of ripple current fluctuations at approximately 120 Hz.

AC ripple filtering is a particularly relevant application for the consideration of structured electrodes and involves the filtering of high order harmonics to protect against electrical power surges and spikes [26]. Such filtering has been shown to be critical for the efficient exploitation of electrical energy generated by photovoltaics or wind turbines with intermittent renewable sources, with the ripples being caused by uncontrollable sunshine or wind flow [22]. To date, aluminium electrolytic capacitors (AECs) are the most common ripple filters due to their extremely high power densities ( $100\text{--}1000\text{ kW kg}^{-1}$ ), although their low energy densities ( $0.01\text{--}0.1\text{ Wh kg}^{-1}$ ) results in bulky AECs taking up large volume in electronic circuits and packs [32]. On the other hand, although there have been attempts to use supercapacitors for AC ripple filtering, their frequency response is generally

considered too slow. For example, commercial supercapacitors using activated carbon electrodes behave comparably to a resistor rather than a capacitor at  $> 1\text{ Hz}$  frequency, far below the required operating frequency [17,25], and has led to recent work on the synthesis of supercapacitors using contact glow discharge electrolysis [2,3] and unstructured mixes of carbon nanofibres [31] for power line applications.

The restricted capacity performance at high frequencies is principally due to impeded mobility of the diffusing ions that carry charge through the tortuous pore structure of the electrode: overcoming or delaying this problem is addressed in this paper. In particular, it is noted that since the ionic current flow across an electrode is non-uniform (following from the diffusive nature of the electrochemical equations), a non-uniform electrode diffusivity could be exploited to promote overall current flow across an electrode. We develop a general framework to describe structured (or layered in this case) electrodes, which is material independent, and based on a consideration of the fundamental electrochemical dynamical equations. It is expected that any benefits of structured electrodes for supercapacitor dynamics will be most apparent for thick electrodes ( $\approx 100\text{ }\mu\text{m}$ ) where diffusion limitations are most pronounced but are otherwise advantageous for volumetric energy density.

Most studies on structured electrodes are simulation based due to a previous lack of an appropriate controlled manufacturing process. However, such processes are now emerging at the laboratory and translational length-scale, based on variations of slurry casting or spray printing [20,23]. Simulation-based results have focused on the optimal design of layered electrodes [12,16,18,28–30,34], and a typical result is the potential for a 61% reduction in Ohmic drop [16]. Similarly, a multi-objective framework has been used in Ref. [29] to discuss the merits of structured electrodes, with metrics such as the standard deviation in the overpotential and resistance being compared [29]. Some of the claimed merits of structured electrodes were refuted in Ref. [11], where simulations of constant current and pulse charging were used to show that many of the aforementioned benefits could be obtained by a judicious choice of porosity in a conventional single layer electrode. In contrast in this paper, the benefits of electrode layering lies in their ability to promote ion mobility across an electrode under high-frequency dynamic currents where diffusion limitations dominate deliverable capacity.

This paper compares experimental supercapacitor impedance and other data with simulation results to explain the mechanisms and limitations of charge storage in layered electrodes. The novelty of the work lies in: (1) An improved electrochemical model for electric double layer supercapacitors allowing for structured electrodes composed of layers of different material properties; (2) The comparison of the model predictions with experimental electrical impedance spectroscopy (EIS) data; and (3) detailed interpretation of real and imaginary capacitance plots for layered electrodes. We conclude: (1) Layering introduces two knee frequencies in the real capacitance that can be manipulated advantageously; (2) Layering can increase the capacity for high frequency operation; (3) Layering decreases capacity at lower frequencies but may also reduce losses; and (4) Electrode response is surprisingly insensitive to some of the details of the layer configuration.

## 2. Electrochemical modelling of structured electrodes

The model develops the electrochemical equations of [13,36] to account for electrodes comprised of two discrete electrode sub-layers.

### 2.1. Electrochemical equations

The model's spatio-temporal variables and parameters are given in Tables 1 and 2. The model equations are given in Table 3 and the boundary conditions are given in Table 4. The electrochemical assumptions of the model are outlined in Ref. [36] and include the

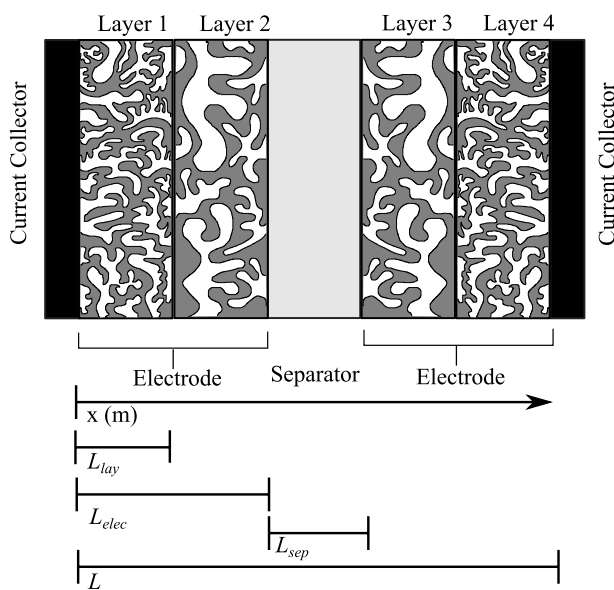


Fig. 2. Illustration of a supercapacitor with structured electrodes. The porous electrodes are formed of two layers with different material properties. The thicknesses of the two layers can be different.

**Table 1**  
Nomenclature of the structured electrode supercapacitor model.

Spatio-Temporal Variables	
$c_e(x, t)$	Ionic concentration in the electrolyte.
$\phi_s(x, t)$	Potential in the electrode.
$\phi_e(x, t)$	Potential in the electrolyte.
$\phi_{dl}(x, t)$	Double layer potential difference. $\phi_{dl}(x, t) = \phi_s(x, t) - \phi_e(x, t)$ .
$i_e(x, t)$	Electron current in the electrode.
$i_e(x, t)$	Ionic current in the electrolyte.
$i(t)$	Applied current density.
$v(t)$	Measured voltage.
Parameters	
$\varepsilon$	Porosity coefficient.
$D$	Effective Diffusion coefficient.
$C^{sp}$	Specific capacitance.
$\sigma$	Electrode conductivity.
$\kappa$	Electrolyte conductivity.
$R$	Universal gas constant.
$F$	Faradays constant.
$T$	Temperature.
$f = \frac{F}{RT}$	A coefficient.
$K =$	A coefficient.
$\frac{(t_+ - t_-)}{f}$	Transference numbers ( $t_+ + t_- = 1$ ).
$\frac{dq_j}{dq} = -\frac{1}{2}$	Change in $j = \{+, -\}$ electrode surface concentration with charge $q$ .
$S$	Electrode surface area.
$j$	$i(t) = I(t)/S$ where $I(t)$ is current. Parameter subscript for the $j^{th}$ layer.

**Table 2**  
Nomenclature for the lengths and positions of the electrodes.

	Length Notation
$L$	Electrode length.
	Separator length.
	Length of the electrode layer closest to the current collector.
	Supercapacitor length. $L = 2L_{elec} + L_{sep}$ .
	0 m
	$L_{lay}$
	$L_{elec}$
	$L_{elec} + L_{sep}$
	$L - L_{lay}$
	$L$

**Table 3**  
Equations for the electrochemical supercapacitor model with structured electrodes. The equations for the  $j^{th}$  layer are denoted by the subscript  $j$ .

Electrode Layer $j$	Separator
$\varepsilon_j \frac{\partial c_e}{\partial t} + \frac{C_j^{sp}}{F} \left( t_- \frac{dq_+}{dq} + t_+ \frac{dq_-}{dq} \right) \frac{\partial \phi_{dl}}{\partial t} = D_j \frac{\partial^2 c_e}{\partial x^2}$	$\varepsilon_s \frac{\partial c_e}{\partial t} = D_s \frac{\partial^2 c_e}{\partial x^2}$
$C_j^{sp} \frac{\partial \phi_{dl}}{\partial t} = \frac{\sigma_j \kappa_j}{\kappa_j + \sigma_j} \frac{\partial^2 \phi_{dl}}{\partial x^2} + \frac{\sigma_j \kappa_j}{\kappa_j + \sigma_j} \frac{\partial^2 \ln(c_e)}{\partial x^2}$	...

Nernst-Planck expression for the ionic flux and dilute solution theory to describe ion movement within the electrode pores. Pseudo-capacitance effects are ignored in the model, however, these effects are negligible for the high frequencies of interest to this paper ( $\approx 100$  Hz).

Consider the supercapacitor cross-section in Fig. 2, where  $x$  is the spatial co-ordinate traversing the domain from one current collector to the other. The dynamics of each electrode layer are described by the same electrochemical equations, but with each layer having distinct

**Table 4**

Boundary conditions for the supercapacitor model for structured electrodes. Subscript “Left” indicates a derivative pointing into the layer to the left of the interface while “Right” indicates a derivative pointing to the right. Similarly, the subscript “sep” indicates a derivative pointing into the separator and “elec” is a derivative pointing into the electrode.

Current Collector    Electrode	Interface Between Electrode	Electrode    Separator
Layers $j$ and $j + 1$		
$\frac{\partial \phi_s}{\partial x} = -\frac{i}{\sigma_j},$ $\phi_s(0, t) = 0,$	$\sigma_j \frac{\partial \phi_s}{\partial x} \Big _{\text{Left}} = \sigma_{j+1} \frac{\partial \phi_s}{\partial x} \Big _{\text{Right}},$	$\frac{\partial \phi_s}{\partial x} = 0,$
$\frac{\partial \phi_e}{\partial x} = 0,$	$\left[ \kappa_j \frac{\partial \phi_e}{\partial x} + \kappa_j \left( \frac{t_+ - t_-}{f} \right) \frac{\partial \ln c_e}{\partial x} \right] \Big _{\text{Left}} =$ $\left[ \kappa_{j+1} \frac{\partial \phi_e}{\partial x} + \kappa_{j+1} \left( \frac{t_+ - t_-}{f} \right) \frac{\partial \ln c_e}{\partial x} \right] \Big _{\text{Right}},$	$\kappa_j \frac{\partial \phi_e}{\partial x} +$ $\kappa_j \left( \frac{t_+ - t_-}{f} \right) \frac{\partial \ln c_e}{\partial x} = i,$
$\frac{\partial c_e}{\partial x} = 0,$	$D_j \frac{\partial c}{\partial x} \Big _{\text{Left}} = D_{j+1} \frac{\partial c}{\partial x} \Big _{\text{Right}},$	$D_j \frac{\partial c}{\partial x} \Big _{\text{elec}} = D_s \frac{\partial c}{\partial x} \Big _{\text{sep}}.$

parameter values. The electrochemical equations are adopted from Ref. [36], with the subscript  $j$  referring to the  $j^{th}$  electrode layer. For instance,  $\sigma_j$  is the electrode conductivity in the  $j^{th}$  layer. In the electrodes, the electrochemical equations [36] are:

$$\varepsilon_j \frac{\partial c_e}{\partial t} + \frac{C_j^{sp}}{F} \left( t_- \frac{dq_+}{dq} + t_+ \frac{dq_-}{dq} \right) \frac{\partial (\phi_s - \phi_e)}{\partial t} = D_j \frac{\partial^2 c_e}{\partial x^2}, \quad (1a)$$

$$C_j^{sp} \frac{\partial (\phi_s - \phi_e)}{\partial t} = \frac{\partial i_e}{\partial x}, \quad (1b)$$

$$\frac{\partial \phi_s}{\partial x} = -\frac{i - i_e}{\sigma_j}, \quad (1c)$$

$$\frac{\partial \phi_e}{\partial x} + \left( \frac{t_+ - t_-}{f} \right) \frac{\partial \ln(c_e)}{\partial x} = -\frac{i_e}{\kappa_j}. \quad (1d)$$

The first equation (1a) describes the diffusion of the electrolyte ions with a source term due to the double layer. The second equation (1b) accounts for the relaxation of the double layer. The third equation (1c) is Ohm’s law for the electrode and the fourth equation (1d) is the Nernst-Planck equation for the electrolyte. These four equations can be simplified by substituting for  $i_e(x, t)$

$$\varepsilon_j \frac{\partial c_e}{\partial t} + \frac{C_j^{sp}}{F} \left( t_- \frac{dq_+}{dq} + t_+ \frac{dq_-}{dq} \right) \frac{\partial (\phi_s - \phi_e)}{\partial t} = D_j \frac{\partial^2 c_e}{\partial x^2}, \quad (2a)$$

$$C_j^{sp} \frac{\partial (\phi_s - \phi_e)}{\partial t} = \sigma_j \frac{\partial^2 \phi_s}{\partial x^2}, \quad (2b)$$

$$\sigma_j \frac{\partial \phi_s}{\partial x} + \kappa_j \frac{\partial \phi_e}{\partial x} + \kappa_j \left( \frac{t_+ - t_-}{f} \right) \frac{\partial \ln(c_e)}{\partial x} + i = 0. \quad (2c)$$

But, the algebraic constraint of (2c) complicates any analysis of a model synthesized from this set of equations, making the layered electrode design problem intractable. To eliminate this constraint, a further substitution is introduced by adding and subtracting  $\kappa_j \partial \phi_s / \partial x$  to (2c) giving:

$$\frac{\partial \phi_s}{\partial x} + \frac{\kappa_j}{(\sigma_j + \kappa_j)} \frac{\partial (\phi_e - \phi_s)}{\partial x} + \frac{\kappa_j}{(\sigma_j + \kappa_j)} \left( \frac{t_+ - t_-}{f} \right) \frac{\partial \ln(c_e)}{\partial x} + \frac{i}{(\sigma_j + \kappa_j)} = 0, \quad (3)$$

which can be differentiated in  $x$

$$\sigma_j \frac{\partial^2 \phi_s}{\partial x^2} = \frac{\sigma_j \kappa_j}{(\sigma_j + \kappa_j)} \frac{\partial^2 (\phi_s - \phi_e)}{\partial x^2} - \frac{\sigma_j}{(\sigma_j + \kappa_j)} \left( \frac{t_+ - t_-}{f} \right) \frac{\partial^2 \ln(c_e)}{\partial x^2}. \quad (4)$$

Substituting (4) back into the RHS of (2b) puts the electrochemical supercapacitor model into the state-space form

$$\frac{\partial c}{\partial t} + \frac{C_j^{\text{sp}}}{\varepsilon_j F} \left( t_- \frac{dq_+}{dq} + t_+ \frac{dq_-}{dq} \right) \frac{\partial(\phi_s - \phi_e)}{\partial t} = \frac{D_j}{\varepsilon_j} \frac{\partial^2 c_e}{\partial x^2}, \quad (5a)$$

$$\frac{\partial \varphi_{dl}}{\partial t} = \frac{\sigma_j \kappa_j}{C_j^{\text{sp}} (\sigma_j + \kappa_j)} \frac{\partial^2 \varphi_{dl}}{\partial x^2} - \frac{\sigma_j}{C_j^{\text{sp}} (\sigma_j + \kappa_j)} \left( \frac{t_+ - t_-}{f} \right) \frac{\partial^2 \ln(c_e)}{\partial x^2}. \quad (5b)$$

This set of equations describes the same set of dynamics as [36], but does not contain algebraic equations. It has a state-space of  $(c_e, \phi_{dl})$  and can be readily analysed and simulated [13].

In the separator, there is only one dynamic equation, that for electrolyte diffusion

$$\varepsilon_s \frac{\partial c_e}{\partial t} = D_s \frac{\partial^2 c_e}{\partial x^2}, \quad (6)$$

with the subscript  $s$  indicating the separator, since the double layer does not exist in the separator as it is an electrical insulator.

## 2.2. Boundary conditions

The model boundary conditions are also inferred from Ref. [36] and are given in Table 4, with the exception of those at the electrode sub-layer to sub-layer interface, which are introduced here. The boundary conditions on the electrolyte ionic concentration  $c_e$  ensure that the supercapacitor is a closed system, with no ions leaving “through” the current collector and a constant ionic flux is imposed at the separator and across the electrode layer interfaces. The boundary conditions on the double layer potential  $\phi_{dl}$  were inferred from those on the potentials in the solid (active and electronical conductive materials) electrode  $\phi_s$  and those in the electrolyte  $\phi_e$ . The boundary conditions on the solid electrode potential  $\phi_s$  enforced all the current to be flowing through the solid phase at the current collectors (with  $i_s = i$ ) and in the liquid phase at the separator ( $i_s = 0$ ). Across the electrode sub-layers, it was assumed that current was conserved i.e.  $i_s|_{\text{Left}} = i_s|_{\text{Right}}$  where Left and Right are respectively subscripts denoting currents flowing from the left and right across the layer boundary. Likewise, the boundary conditions on  $\phi_e$  ensured that the current in the electrolyte was zero at the current collectors ( $i_e = 0$ ), equalled the full current at the separator ( $i_e = i$ ) and was conserved across the electrode layers  $i_e|_{\text{Left}} = i_e|_{\text{Right}}$ . These inter-layer boundary conditions contrast with those from Ref. [29] where no current conservation was imposed.

## 2.3. Voltage

The voltage  $v$  of the supercapacitor is defined as the solid phase potential difference between the two current collectors

$$v(t) = \phi_s(0, t) - \phi_s(L, t). \quad (7)$$

But, this expression is not a function of the state-space  $(c_e, \phi_{dl})$ . To obtain such an expression, the voltage equation (7) was first written as the sum of the potential differences across each layer

$$v(t) = - \sum_{j=0}^4 \phi_s(L_{j+1}, t) - \phi_s(L_j, t). \quad (8)$$

The positions  $L_j$  correspond to the layer interfaces and are defined in Table 2 with  $\{L_0, L_5\}$  at the current collectors,  $\{L_1, L_4\}$  at the layer interface positions and  $\{L_2, L_3\}$  at the end points of the separator. This expression assumes that the sub-layering configuration in each electrode is mirrored but could be easily modified if this was not the case. Equation (8) can be represented as a path integral of the potential gradient

$$v(t) = - \sum_{j=0}^4 \int_{L_j}^{L_{j+1}} \frac{\partial \phi_s(x, t)}{\partial x} dx. \quad (9)$$

Substituting the expression for  $\partial \phi_s(x, t) / \partial x$  from (3) into this summation, gives

$$v(t) = \sum_{j=0}^4 \int_{L_j}^{L_{j+1}} - \frac{\kappa_j}{(\sigma_j + \kappa_j)} \frac{\partial \varphi_{dl}(x, t)}{\partial x} + \frac{\kappa_j}{(\sigma_j + \kappa_j)} \left( \frac{t_+ - t_-}{f} \right) \frac{\partial \ln(c_e(x, t))}{\partial x} + \frac{i}{(\sigma_j + \kappa_j)} dx \quad (10)$$

which can be evaluated exactly

$$v(t) = \sum_{j=0}^4 \left[ - \frac{\kappa_j}{(\sigma_j + \kappa_j)} \varphi_{dl}(x, t) + \frac{\kappa_j}{(\sigma_j + \kappa_j)} \left( \frac{t_+ - t_-}{f} \right) \ln(c_e(x, t)) + \frac{ix}{\sigma_j + \kappa_j} \right] \Big|_{x=L_j}^{x=L_{j+1}} \quad (11)$$

to give the voltage as a function of the states  $(\phi_{dl}, c_e)$ .

## 3. Parameter estimation of the electrochemical model

Accurate parameter estimates were required for the model simulations to represent experimental data and to give predictive power. For parameter identification and simulation purposes, the PDE equations in (5) were first discretised in space using the spectral collection method of [13], with the discretised model parameters then identified using the procedure outlined in Ref. [14].

The parameter estimation problem can be cast as the solution to the least squares optimisation

$$\theta^* = \min_{\theta} \|\hat{Z}(\theta) - Z\|_2^2 \quad (12)$$

where  $\theta = \{\kappa_j, C_j^{\text{sp}}, \sigma_j, L_{\text{elec}}, L_{\text{sep}}, L_{\text{lay}}, S, t_+, \varepsilon_j, D_j\}$  are the models parameters,  $\theta^*$  is the optimal parameter choice that minimises the distance between simulation and data,  $\hat{Z}(\theta)$  is the simulated response and  $Z$  is a set of data points of bi-layered supercapacitors synthesized with the method outlined in Section II-A.

In this paper, electrical impedance spectroscopy (EIS) data is used for the identification, with EIS giving the frequency domain mapping from current  $I(j\omega)$  to voltage  $V(j\omega)$  as

$$V(j\omega) = G(j\omega)I(j\omega). \quad (13)$$

A local impedance function for the electrochemical model was obtained by linearising the spatially discretised model equations around an equilibrium point and applying the Laplace transform. EIS data was used for the identification because in comparison with time domain constant-current/constant voltage data, it gives a more complete characterisation of supercapacitor dynamics. Solving (12) with  $\hat{Z}(\theta)$  as the impedance function gave a reasonable match to experimental data, with the estimated parameters given in Tables 5 and 6.

### 3.1. Experimental set-up

The electrochemical model parameters were identified from experimental data of bi-layered supercapacitors. The bi-layer electrodes were synthesized using a scalable suspension atomization and automatic spray deposition processing technique developed previously [20,37]. Two types of aqueous suspension were used, one containing TiO<sub>2</sub> nanoparticles and another containing carbon nanotubes (CNTs), were prepared separately through sonication. The choice of CNTs and TiO<sub>2</sub> as the electrode materials was based on their known supercapacitor behaviour and good performance from previous experimental studies [19,21]. Besides having distinctly different material properties that may make layering effects identifiable, the two materials are also interesting from a manufacturing point of view, since the TiO<sub>2</sub> is significantly

**Table 5**

Parameters for the supercapacitor model that hold in each domain.

Parameter	Value	Units
Global Parameters		
$L$	37	$\mu\text{ m}$
$t_+$	0.625	
$S$	$1.13 \times 10^{-4}$	$\text{M}^2$
$\frac{dq_+}{dq_-} = \frac{dq_-}{dq_+}$	-0.5	
$T$	298	K
Separator Parameters		
$L_s$	80	$\mu\text{ m}$
$\varepsilon_s$	0.05	
$D_s$	$1 \times 10^{-11}$	$\text{m}^2 \text{ s}^{-1}$
Layer Setup 1		
$L_{\text{lay}}$	32	$\mu\text{ m}$
Layer Setup 2		
$L_{\text{lay}}$	5	$\mu\text{ m}$

**Table 6**

Material specific parameters.

Parameter	TiO <sub>2</sub>	Nanotubes	Units
$\varepsilon$	0.26	0.083	
$\kappa$	0.018	0.0178	$\text{S m}^{-1}$
$\sigma$	22	340	$\text{S m}^{-1}$
$C^{\text{sp}}$	$3.28 \times 10^7$	$2.30 \times 10^7$	$\text{F m}^{-3}$
$D$	$2.25 \times 10^{-13}$	$8.39 \times 10^{-12}$	$\text{m}^2 \text{ s}^{-1}$

cheaper than CNTs, so in general the CNT fraction in an electrode should be minimised. The results presented here then represent a means to “dope” cheap TiO<sub>2</sub> with high performance (but expensive) CNTs to bring performance benefits at the macro-scale using the advanced manufacturing methods described. The suspensions were pumped into separate nozzles, atomized into micro-droplets by compressed air, and consecutively sprayed to form two layers of the electrode on a current collector maintained at 100 °C on a heated vacuum stage-chuck. Any fugitive water in the spray suspensions evaporated continuously on the heated stage as the electrodes formed. The nozzles moved in a pre-programmed zig-zag pattern along X and Y directions at 20 mm s<sup>-1</sup> to spray an area up to 20 cm × 20 cm. The spray processing was performed in a cross flow of air in a fume cupboard.

The electrode layer thicknesses were chosen as given in setup 1 in Table 5, with the electrode sub-layer closest to the current collector composed of CNTs while the sub-layer closest to the separator was composed primarily of TiO<sub>2</sub> particulate. The electrode mass loading was 2.1–2.6 mg cm<sup>-2</sup>, the electrolyte was 1 M H<sub>2</sub>SO<sub>4</sub> and stainless-steel foil (type 304, Zapp Precision Metals) current collectors were used. Sulphuric acid was chosen as the electrolyte primarily because it is one of the most common aqueous protic electrolytes for supercapacitors, with relatively high ionic conductivity of 0.35 S cm<sup>-1</sup> at 1 M [7]. EIS was conducted on a Reference 600/EIS300 Gamry potentiostat/galvanostat operated within the  $2 \times 10^5 - 10^2$  Hz frequency range with a  $\pm 5$  mV rms AC voltage, operated at open circuit voltage at room temperature.

### 3.2. EIS simulations: comparison to data

A comparison between the impedance functions of the electrochemical model and the experimental data under ideal conditions is shown in Fig. 4. Here, Fig. 4a plots the Argand diagram of the impedance function of the bi-layered electrodes while Fig. 4b and c respectively show the corresponding real and imaginary parts as a function of frequency. There was a tolerably good fit between the data and simulation across the frequency range  $10^{-2} - 10^2$  rad s<sup>-1</sup>. To show that the

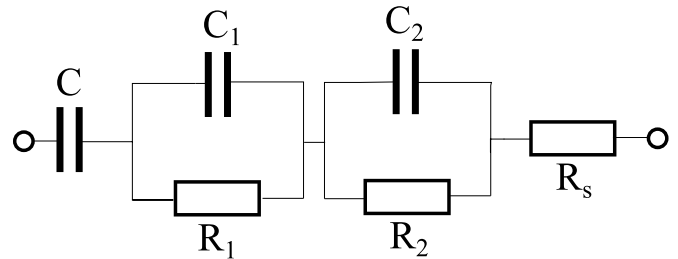
identification avoided over-fitting, the model was validated in Fig. 8 against data with the position of the sub-layers within the electrode swapped around, showing that the model was able to maintain a good fit to experimental data.

### 3.3. Equivalent circuit synthesis

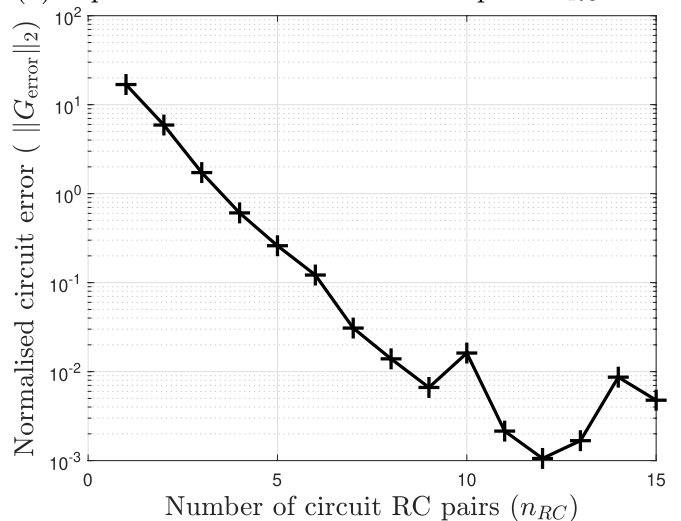
In supercapacitor modelling, it is often desirable to extract an equivalent circuit from the impedance function to characterise the response. Such circuits are now synthesized directly from the impedance function of the electrochemical model  $G(s)$  using the method from Ref. [15]. In particular, circuits with the structure of Fig. 3a are generated for different RC pair numbers  $n_{RC}$ . Note that since the impedance of a diffusing system is transcendental, fractional capacitances are often used in these circuits [4], although fractional components are not realisable from the discretised electrochemical model. Solving the coupled linearised electrochemical PDEs directly for the analytic impedance function would enable these fractional capacitances to be computed, but this is left to future work.

The considered circuits admit the state-space realisation

$$\begin{bmatrix} \dot{x}_c \\ \dot{x}_1 \\ \vdots \\ \dot{x}_{n_{RC}} \end{bmatrix} = \begin{bmatrix} 0 & & & \\ & -\frac{1}{R_1 C_1} & & \\ & & \ddots & \\ & & & -\frac{1}{R_{n_{RC}} C_{n_{RC}}} \end{bmatrix} \begin{bmatrix} x_c \\ x_1 \\ \vdots \\ x_{n_{RC}} \end{bmatrix} + \begin{bmatrix} \frac{1}{C} \\ \frac{1}{C_1} \\ \vdots \\ \frac{1}{C_{n_{RC}}} \end{bmatrix} i(t), \quad (14a)$$

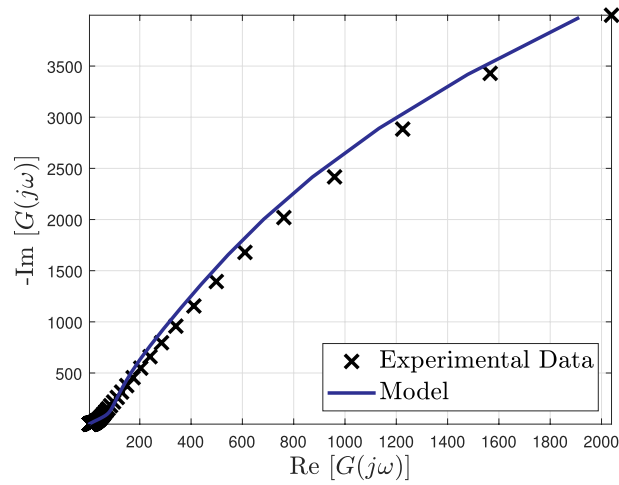
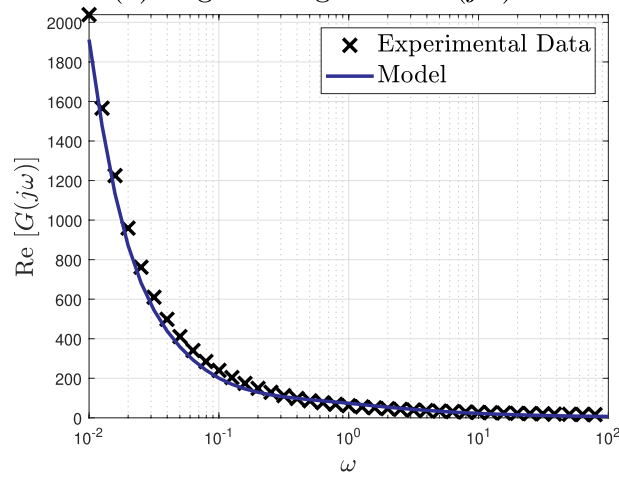
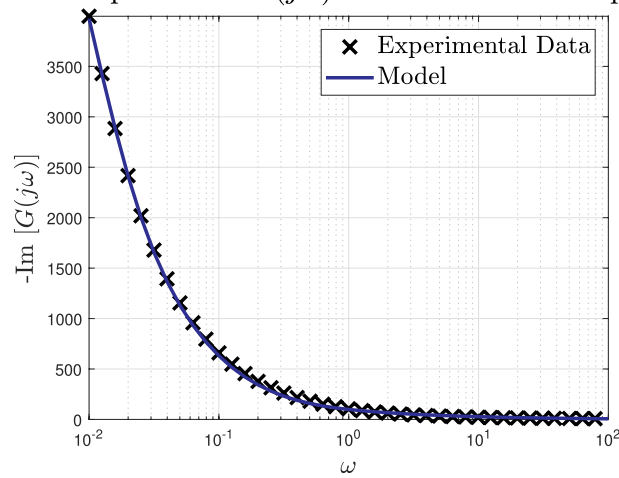


(a) Equivalent circuit with two RC pairs  $n_{RC} = 2$ .



**Fig. 3.** The two RC pair equivalent circuit whose parameters were synthesized directly from the discretised electrochemical model is shown in Fig. 3a. The error between the impedance of the linearised and discretised electrochemical model and the synthesized circuits as a function of the number of RC pairs  $n_{RC}$  is shown in Fig. 3b.



(a) Argand diagram of  $G(j\omega)$ .(b) Real component of  $G(j\omega)$  as a function of frequency.(c) Imaginary component of  $G(j\omega)$  as a function of frequency.

**Fig. 4.** Experimental and simulated impedance function plots for a supercapacitor with structured bi-layer electrodes in the set-up 1 configuration, with a layer of carbon nanotubes (CNTs) close to the current collector and a layer of  $\text{TiO}_2$  particulate close to the separator.

$$v(t) = x_c + \sum_{j=1}^{n_c} x_j + R_s i(t) \quad (14b)$$

to generate an impedance

$$G_{\text{circ}}(j\omega) = \frac{1}{C_j \omega} + R_s + \sum_{j=1}^{n_c} \frac{1}{C_j(j\omega + R_j C_j)}. \quad (15)$$

To extract the circuit parameters, balanced truncation [15] is applied to  $G(s)$  and the resulting state-space system is then transformed into (14). In this manner, the circuit components are directly linked to the electrochemical parameters, for example the porosity and electrolyte conductivity. The circuit of Fig. 3a with  $n_{RC} = 2$  can then be directly synthesized, with  $C = 0.0573$  C,  $C_1 = 0.0138$  C,  $C_2 = 0.0277$  C,  $R_1 = 213.924$   $\Omega$ ,  $R_2 = 4.740 \times 10^3$   $\Omega$  and  $R_s = 3.801$   $\Omega$ .

To evaluate the diminishing importance of the number of RC pairs to the circuit accuracy, the following error metric is introduced

$$\|G_{\text{error}}\|_2 = \frac{1}{n_\omega} (\| \text{Im}[G(j\omega) - G_{\text{circ}}(j\omega)] \|_2 + \| \text{Re}[G(j\omega) - G_{\text{circ}}(j\omega)] \|_2) \quad (16)$$

In essence, this metric measures the average error between  $G_{\text{circ}}$  (for a given number of RC pairs  $n_c$ ) and  $G$  evaluated over the frequency points  $\omega \in \mathbb{R}^{n_\omega}$ , with  $n_\omega$  being the number of evaluated frequencies. Fig. 3b plots the error  $\|G_{\text{error}}\|_2$  as a function of the number of circuit RC pairs  $n_{RC}$ , showing that low order circuits gave sufficient accuracy.

#### 4. Real and imaginary capacitance

This section investigates how the introduction of the sub-layers within the electrodes affected the real and imaginary capacitance [24, 35]. These capacitances are often used as performance metrics for supercapacitors and are obtained from the EIS response by decomposing the impedance function into real and imaginary parts according to

$$G(j\omega) = G'(\omega) + jG''(\omega). \quad (17)$$

Primes are used to denote real components and double primes denote imaginary components. This function can be represented as a *supercapacitance*  $C(\omega)$  such that

$$G(j\omega) = \frac{1}{j\omega C(\omega)}. \quad (18)$$

The reason for expressing  $G(j\omega)$  in this manner is to obtain a frequency domain form of the capacitance equation  $Q = Cv$ , where  $Q$  is the stored charge and  $C$  is the device capacitance. Through some rearranging [35], it follows that the *supercapacitance* has the form

$$C(\omega) = C'(\omega) - jC''(\omega) \quad (19)$$

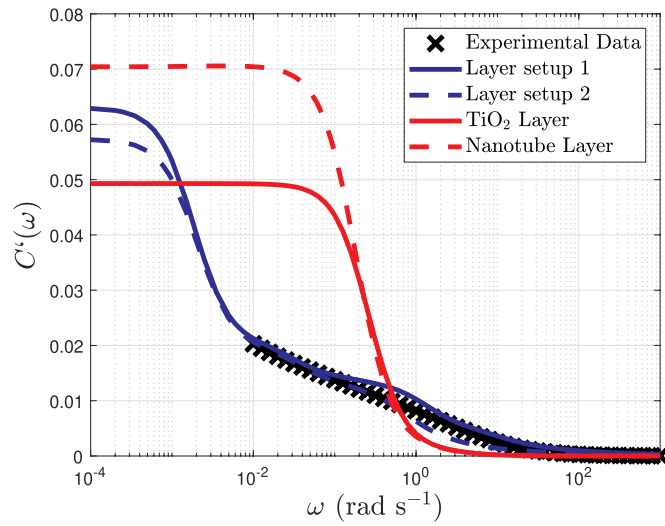
where  $C'(\omega)$  is the real capacitance

$$C'(\omega) = -\frac{G''(\omega)}{\omega |G(\omega)|^2} \quad (20)$$

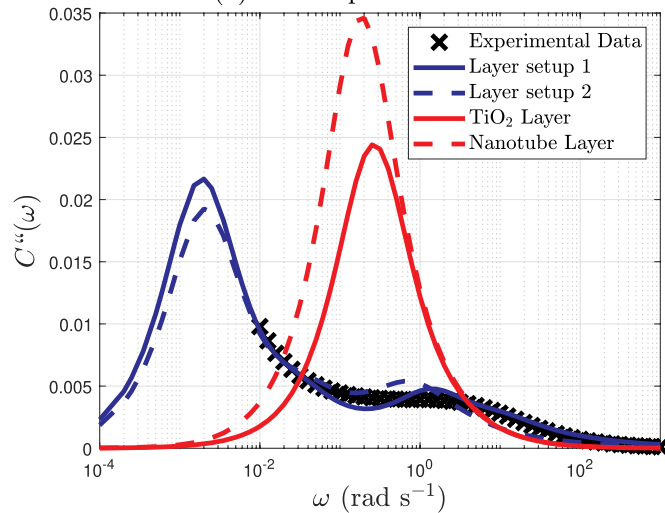
and  $C''(\omega)$  is the imaginary capacitance

$$C''(\omega) = \frac{G'(\omega)}{\omega |G(\omega)|^2}. \quad (21)$$

According to Ref. [35], the real part  $C'(\omega)$  is effectively the capacitance while the imaginary capacitance  $C''(\omega)$  corresponds to energy



(a) Real capacitance.



(b) Imaginary capacitance.

**Fig. 5.** Capacitances as a function of frequency. Simulations for structured electrodes are shown in blue. Layer setup 1 corresponds to an outer layer of carbon nanotubes and an inner layer of  $\text{TiO}_2$  particulate. Layer setup 2 has the order of these layers swapped around. Simulations for the equivalent single layer electrodes are shown in red. Experimental data is shown in black for layer setup 1.

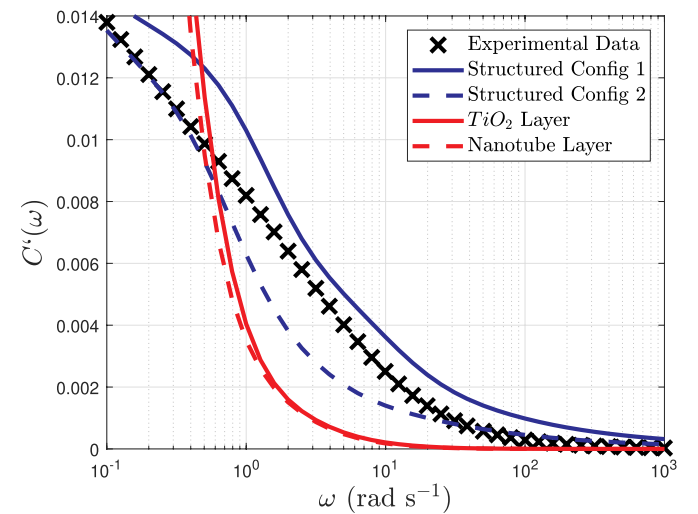


**Fig. 6.** Real capacitances of Fig. 5a in the high frequency range. Introducing layers into the electrodes strengthens the storage capability at these frequencies.

dissipated by irreversible losses. Optimising over these capacitances is often said to be equivalent to optimising over the Pareto front of the Ragone plot [9].

#### 4.1. Real & imaginary capacitance: comparison to data

Fig. 5 shows simulated real and imaginary capacitance as a function

of frequency for various supercapacitors. For these simulations, set-up 1 had a  $32 \mu\text{m}$  thick sub-layer closest to the current collector composed primarily of  $\text{TiO}_2$  particulate and a  $5 \mu\text{m}$  thick sub-layer closest to the separator primarily comprising of CNT. Set-up 2 had the position of the sub-layers swapped, with the  $5 \mu\text{m}$  thick CNT sub-layer closest to the current collector and the  $32 \mu\text{m}$  thick  $\text{TiO}_2$  sub-layer closest to the separator. Experimental data for set-up 1 is shown in black and

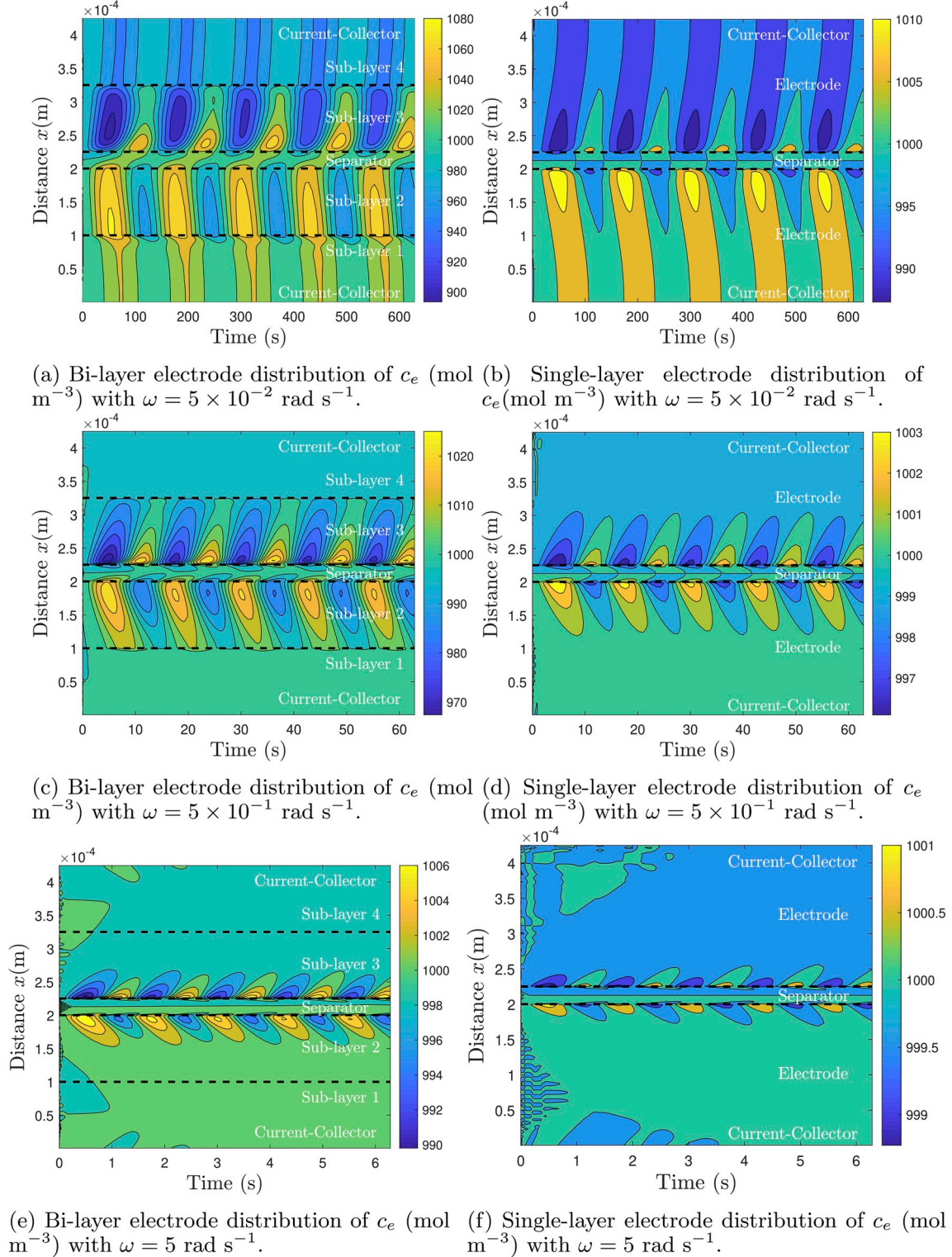


**Fig. 7.** Evolution of the electrolyte ionic concentration  $c_e$  ( $\text{mol m}^{-3}$ ) for a sinusoidal charge/discharge current  $I(t) = 10^{-3} \sin(\omega t)$  with different frequencies  $\omega$ . Simulations for both  $200 \mu\text{m}$  thick bi-layer  $\text{TiO}_2/\text{CNT}$  structured electrodes (left) and  $200 \mu\text{m}$  thick single layer CNT-only electrodes (right) are shown.



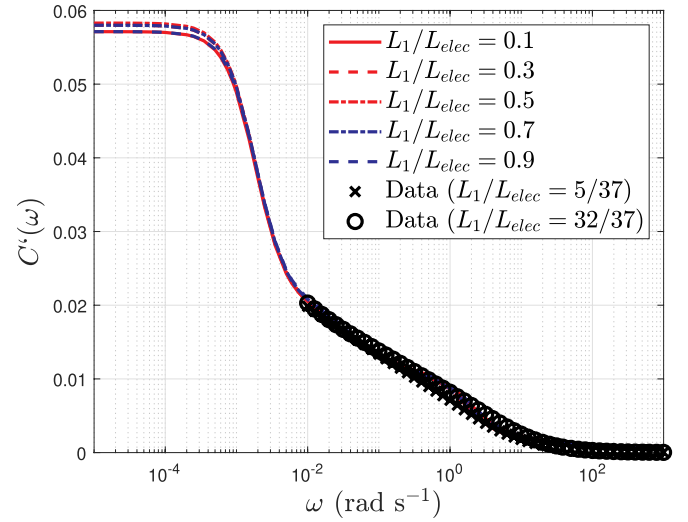
corresponding simulation results are shown in blue. Equivalent supercapacitors with electrodes comprising only of  $\text{TiO}_2$  and only of CNT are shown in red.

The most noticeable feature in the capacitances plots of the structured bi-layer electrodes in Fig. 5 was the presence of two peaks in the imaginary capacitance plots and the corresponding two knee frequencies in the real capacitance plots. While there was only a single peak in the  $\text{TiO}_2$ -only and CNT-only electrodes. The additional peak is however consistent with the recent result in Ref. [10] which also mapped electrochemical equations to EIS results, but for electrodes with a linearly varying porosity fraction through the electrode thickness. The authors in Ref. [10] warned that such peaks may be misinterpreted as additional electrochemical effects [6], but are actually diffusion based, and the results presented here reinforce this conclusion. We verify the presence of two peaks in the case of sub-layered electrodes which are often associated to “constant phase elements” [35], with a physical explanation for such elements remaining a topic of dispute [1]: explanations include surface roughness, distributions of reaction rates and non-uniform current distributions within the electrode. The simulations and experiments here suggest that the presence of the peaks was due to the coupled diffusion between/within the sub-layers.

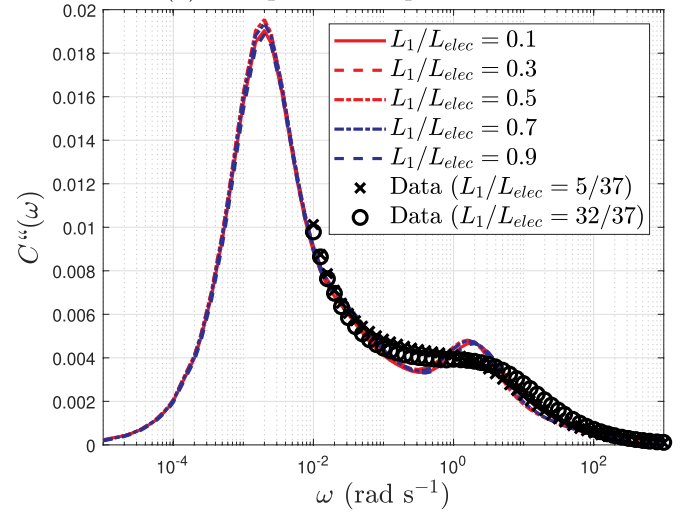
Fig. 5 also shows the impact on the frequency dependant capacity caused by layering. Focusing first in the high frequency region  $10^0 \leq \omega \leq 10^2$  shown in more detail in Fig. 6, layering increased the capacity in this region. This was due to the two knee frequencies of the sub-layered electrodes and corresponding to the frequency region where diffusion limitations in the electrolyte dominate performance. The presence of two knee frequencies was most likely due to two different effective diffusion coefficients from the electrode sub-layers and their coupling via the boundary conditions at the internal sub-layer interface. This gives encouragement for the use of structured electrodes in applications with high frequency charging. However, the double knee profile also resulted in a drop in capacity in the frequency region  $10^{-3} \leq \omega \leq 10^0$ , albeit with lower losses. Finally, for DC charging at  $\omega \approx 0$ , where diffusion effects are insignificant, the capacity of the layered electrode sensibly was an average of the two single layer cases. This suggests that sandwiching relatively cheap  $\text{TiO}_2$  based electrodes with a smaller fraction of more expensive high performance CNTs could increase capacity at DC over a  $\text{TiO}_2$  electrode and provide additional capacity in the high frequency region.

This high frequency capability of the structured or bi-layer electrodes is explained in terms of increased ion mobility in Fig. 7. This figure shows simulated ionic concentration distributions in space and time for both a supercapacitor with bi-layer  $\text{TiO}_2/\text{CNT}$  structured electrodes and a supercapacitor with CNT-only electrodes. Relatively thick electrode sub-layers of  $100 \mu\text{m}$  were used for these simulations to draw out differences more clearly, with single material electrodes of  $200 \mu\text{m}$  thickness and a  $20 \mu\text{m}$  thick separator in all cases. The bi-layered supercapacitors were charged by a sinusoidal current of amplitude  $10^{-3} \text{ A}$  at frequencies of  $5 \times 10^{-2} \text{ rad s}^{-1}$ ,  $5 \times 10^{-1} \text{ rad s}^{-1}$  and  $5 \text{ rad s}^{-1}$ .

Fig. 7 illustrates the increased ion mobility in the bi-layered electrodes seen in the model simulations. At low charging frequencies, the response of the bi-layered electrodes was similar to that of the CNT-only electrodes, with the electrolyte ions diffusing across the whole electrode. But, as the charging frequency was increased, the effect of the sub-layers became more pronounced. The layering created a region around the separator where ion mobility was amplified and reduced the effective length of the layered electrode to that of the inner layer. This thin pseudo-electrode explained the improved capability at high frequencies. Also, since the voltage expression (11) contained contributions from the electrolyte concentration  $c_e$  at each of the layer interfaces, this increased ion mobility affected the voltage response. These simulations explain the double knee frequencies (due to the two diffusion time constants from the two sub-layers) and the increased performance at high charging frequencies (due to the increased ion mobility across the supercapacitor)



(a) Sweep of real capacitance.



(b) Sweep of imaginary capacitance.

Fig. 8. A sweep of real and imaginary capacitances over the length ratios of the outer layers  $L_1 = L_4$  to the electrode  $L_{elec} = 37 \mu\text{m}$ . The outer layers are nanotubes while the inner layers are  $\text{TiO}_2$ . Two sets of experimental data are also shown.

in the experimental impedance plots. It is conjectured that this effect can be extrapolated to  $n$  sub-layers where the effect may be amplified further.

The model framework described here has sufficient flexibility that it can be used to guide designs for improved functionality, through the considerably widened supercapacitor design space facilitated by structured electrodes (and the corresponding manufacturing technologies). Critically, changes in model parameters can be directly linked to changes in energy storage performance. Fig. 8a and b explore this idea by showing device capacitances as a function of the ratios of the electrode sub-layer thicknesses. Noticeably, for all sub-layer thickness ratios, the capacitance plots were qualitatively similar, with the most significant difference in capacitance being when the layers were the same thickness but had their position swapped, as was shown earlier in Fig. 5a and b. This relative insensitivity to the sub-layer thickness ratios, seen in both the model simulations and the experimental data, implies that there is no distinct optimal thickness ratio, although this conclusion may not hold for different electrode configurations, especially as electrode thicknesses increase.

## 5. Conclusions

A model describing ionic diffusion and electric double layer capacitance dynamics was developed, tuned and validated against EIS data, with the tuned model parameters obtained from the solution of a least mean squares problem. Real and imaginary capacitances for the bi-layered structured electrodes contained two knee frequencies, which could be manipulated by changes in the electrode design to increase the capacitance at high frequencies. Model simulation results showed that these increased capacitances derived from increased ion mobility facilitated by sub-layering and the nature of the resulting coupled diffusion between sub-layers.

Extensions of this work will focus on Li-ion battery electrodes, where the design flexibility of the layering could be exploited to promote reaction rate (insertion/de-insertion of Li-ions) homogeneity across the thickness of the electrodes. As well as increasing the capacity during fast charging, homogenisation of electrode charge distribution may reduce capacity degradation.

## Acknowledgement

The authors would like to thank the UK Engineering and Physical Research Council (EPSRC) for financial support of this research through grant EP/005411/1-“Structured electrodes for improved energy storage” and EPSRC UKRI Innovation Fellowship EP/S001239/1 “Novel Manufacturing Approaches to Next Generation Batteries”.

## References

- [1] M.S. Abouzari, F. Berkemeier, G. Schmitz, D. Wilmer, On the physical interpretation of constant phase elements, *Solid State Ionics* 180 (14) (2009) 922–927.
- [2] A. Allagui, A.S. Elwakil, M.E. Fouda, A.G. Radwan, Capacitive behavior and stored energy in supercapacitors at power line frequencies, *J. Power Sources* 390 (2018) 142–147.
- [3] A. Allagui, A.S. Elwakil, Z. Said, M.A. Abdelkareem, D. Zhang, Band-pass filter and relaxation oscillator using electric double-layer capacitor, *ChemElectroChem* 5 (23) (2018) 3793–3798.
- [4] A. Allagui, T.J. Freeborn, A.S. Elwakil, M.E. Fouda, B.J. Maundy, A.G. Radwan, Z. Said, M.A. Abdelkareem, Review of fractional-order electrical characterization of supercapacitors, *J. Power Sources* 400 (2018) 457–467.
- [5] F. Béguin, V. Presser, A. Balducci, E. Frackowiak, Carbons and electrolytes for advanced supercapacitors, *Adv. Mater.* 26 (14) (2014) 2219–2251.
- [6] A. Bertel, G. Arcolini, C. Nicoletta, P. Piccardo, Effect of non-uniform electrode microstructure in gas diffusion impedance, *ECS Trans.* 68 (1) (2015) 2897–2905.
- [7] M. Boota, Y. Gogotsi, MXene-conducting polymer asymmetric pseudocapacitors, *Adv. Energy Mater.* 9 (7) (2019) 1802917.
- [8] C. Cheng, R. Drummond, S.R. Duncan, P.S. Grant, Micro-scale graded electrodes for improved dynamic and cycling performance of Li-ion batteries, *J. Power Sources* 413 (2019) 59–67.
- [9] T. Christen, M.W. Carlen, Theory of Ragone plots, *J. Power Sources* 91 (2) (2000) 210–216.
- [10] S.J. Cooper, A. Bertel, D.P. Finegan, N.P. Brandon, Simulated impedance of diffusion in porous media, *Electrochim. Acta* 251 (2017) 681–689.
- [11] Y. Dai, V. Srinivasan, On graded electrode porosity as a design tool for improving the energy density of batteries, *J. Electrochem. Soc.* 163 (3) (2016) A406–A416.
- [12] S. De, P.W.C. Northrop, V. Ramadesigan, V.R. Subramanian, Model-based simultaneous optimization of multiple design parameters for lithium-ion batteries for maximization of energy density, *J. Power Sources* 227 (2013) 161–170.
- [13] R. Drummond, D.A. Howey, S.R. Duncan, Low-order mathematical modelling of electric double layer supercapacitors using spectral methods, *J. Power Sources* 277 (2015) 317–328.
- [14] R. Drummond, D.A. Howey, S.R. Duncan, Parameter estimation of an electrochemical supercapacitor model, in: *Proc. Of the European Control Conference, Aalborg, Denmark, 2016*, pp. 1–6.
- [15] R. Drummond, S. Zhao, D.A. Howey, S.R. Duncan, Circuit synthesis of electrochemical supercapacitor models, *J. Energy Storage* 10 (2017) 48–55.
- [16] S. Golmon, K. Maute, M.L. Dunn, A design optimization methodology for Li+ batteries, *J. Power Sources* 253 (2014) 239–250.
- [17] Z.J. Han, C. Huang, S.S. Meysami, D. Piche, D.H. Seo, S. Pineda, A.T. Murdock, P. S. Bruce, P.S. Grant, N. Grobert, High-frequency supercapacitors based on doped carbon nanostructures, *Carbon* 126 (2018) 305–312.
- [18] M.R. Hasyim, D. Ma, R. Rajagopalan, C. Randall, Prediction of charge-discharge and impedance characteristics of electric double-layer capacitors using porous electrode theory, *J. Electrochem. Soc.* 164 (13) (2017) A2899–A2913.
- [19] C. Huang, N.P. Young, P.S. Grant, Spray processing of TiO<sub>2</sub> nanoparticle/ionomer coatings on carbon nanotube scaffolds for solid-state supercapacitors, *J. Mater. Chem.* 2 (29) (2014), 11 022–11 028.
- [20] C. Huang, N.P. Young, J. Zhang, H.J. Snaith, P.S. Grant, A two layer electrode structure for improved Li-ion diffusion and volumetric capacity in Li-ion batteries, *Nano Energy* 31 (2017) 377–385.
- [21] C. Huang, J. Zhang, N.P. Young, H.J. Snaith, P.S. Grant, Solid-state supercapacitors with rationally designed heterogeneous electrodes fabricated by large area spray processing for wearable energy storage applications, *Sci. Rep.* 6 (2016) 25684.
- [22] J. Lin, C. Zhang, Z. Yan, Y. Zhu, Z. Peng, R.H. Hauge, D. Natelson, J.M. Tour, 3-dimensional graphene carbon nanotube carpet-based microsupercapacitors with electrochemical performance, *Nano Lett.* 13 (1) (2012) 72–78.
- [23] L. Liu, P. Guan, C. Liu, Experimental and simulation investigations of porosity graded cathodes in mitigating battery degradation of high voltage lithium-ion batteries, *J. Electrochem. Soc.* 164 (13) (2017) A3163–A3173.
- [24] M. Lu, F. Béguin, E. Frackowiak, *Supercapacitors: Materials, Systems and Applications*, John Wiley & Sons, Weinheim, Germany, 2013.
- [25] J.R. Miller, R. Outlaw, B. Holloway, Graphene double-layer capacitor with AC line-filtering performance, *Science* 329 (5999) (2010) 1637–1639.
- [26] J.R. Miller, R. Outlaw, B. Holloway, Graphene electric double layer capacitor with ultra-high-power performance, *Electrochim. Acta* 56 (28) (2011), 10 443–10 449.
- [27] J.R. Miller, P. Simon, Electrochemical capacitors for energy management, *Sci. Mag.* 321 (5889) (2008) 651–652.
- [28] J. Newman, Optimization of porosity and thickness of a battery electrode by means of a reaction-zone model, *J. Electrochem. Soc.* 142 (1) (1995) 97–101.
- [29] Y. Qi, T. Jang, V. Ramadesigan, D.T. Schwartz, V.R. Subramanian, Is there a benefit in employing graded electrodes for lithium-ion batteries? *J. Electrochem. Soc.* 164 (13) (2017) A3196–A3207.
- [30] V. Ramadesigan, R.N. Methekar, F. Latinwo, R.D. Braatz, V.R. Subramanian, Optimal porosity distribution for minimized ohmic drop across a porous electrode, *J. Electrochem. Soc.* 157 (12) (2010) A1328–A1334.
- [31] Z. Said, A. Allagui, M.A. Abdelkareem, A.S. Elwakil, H. Alawadhi, R. Zannerni, K. Elsaid, Modulating the energy storage of supercapacitors by mixing close-to-ideal and far-from-ideal capacitive carbon nanofibers, *Electrochim. Acta* 301 (2019) 465–471.
- [32] K. Sheng, Y. Sun, C. Li, W. Yuan, G. Shi, Ultrahigh-rate supercapacitors based on electrochemically reduced graphene oxide for AC line-filtering, *Sci. Rep.* 2 (2012) 247.
- [33] P. Simon, Y. Gogotsi, Materials for electrochemical capacitors, in: *Nanoscience And Technology: A Collection of Reviews from Nature Journals*, World Scientific, 2010, pp. 320–329.
- [34] B. Suthar, P.W.C. Northrop, D. Rife, V.R. Subramanian, Effect of porosity, thickness and tortuosity on capacity fade of anode, *J. Electrochem. Soc.* 162 (9) (2015) A1708–A1717.
- [35] P. Taberna, P. Simon, J.-F. Fauvarque, Electrochemical characteristics and impedance spectroscopy studies of carbon-carbon supercapacitors, *J. Electrochem. Soc.* 150 (3) (2003) A292–A300.
- [36] M.W. Verbrugge, P. Liu, Microstructural analysis and mathematical modeling of electric double-layer supercapacitors, *J. Electrochem. Soc.* 152 (5) (2005) D79–D87.
- [37] X. Zhao, B.T. Chu, B. Ballesteros, W. Wang, C. Johnston, J.M. Sykes, P.S. Grant, Spray deposition of steam treated and functionalized single-walled and multi-walled carbon nanotube films for supercapacitors, *Nanotechnology* 20 (6) (2009), 065605.